

Facile Alcohothermal Synthesis, Size-Dependent Ultraviolet Absorption, and Enhanced CO Conversion Activity of Ceria Nanocrystals

Ya-Wen Zhang, Rui Si, Chun-Sheng Liao, and Chun-Hua Yan*

State Key Lab of Rare Earth Materials Chemistry and Applications & PKU-HKU Joint Lab on Rare Earth Materials and Bioinorganic Chemistry, Peking University, Beijing 100871, China

Chao-Xian Xiao and Yuan Kou

College of Chemistry and Molecular Engineering, Peking University, Beijing 100871, China

Received: April 11, 2003; In Final Form: June 14, 2003

Uniform ceria nanocrystals with good crystallinity and high surface areas were prepared by a facile alcohothermal method with the addition of bases (KOH or NaOH), using Ce(III) or Ce(IV) salt as a starting material. The as-prepared nanocrystals were characterized by means of powder X-ray diffraction (PXRD), transmission electron microscopy (TEM), high-resolution TEM (HRTEM), nitrogen adsorption, thermogravimetry and differential thermal analysis (TG-DTA), Fourier transformation infrared spectroscopy (FT-IR), X-ray photoelectron spectroscopy (XPS), and ultraviolet and visible spectroscopy (UV-vis). The ceria crystals had controllable sizes from 2.6 to 6.9 nm estimated by the PXRD line broadening analysis. TEM and HRTEM micrographs showed that the as-prepared ceria nanocrystals have a relatively high degree of crystallinity and low degree of conglomeration under high base concentrations. BET specific surface areas of the as-synthesized ceria nanocrystals were very high ($103\text{--}238\text{ m}^2\text{ g}^{-1}$). XPS spectra indicated that the cerium in the nanocrystals was predominantly tetravalent. UV-vis spectra revealed that both the direct and indirect band gap energies of the as-prepared ceria nanocrystals showed a pronounced blue-shifting due to the quantum confinement effect compared to bulk ceria. And the dielectric confinement effect on the band gap energies was also discussed. The as-prepared ceria nanocrystals supported on $\gamma\text{-Al}_2\text{O}_3$ exhibited a rather lower conversion temperature (559 K) for CO oxidation to CO_2 than that of bulk catalysts prepared by the coprecipitation method. Finally, a hydrolytic alcohothermal mechanism for the preparation of ceria nanocrystals was forwarded.

Introduction

As a functional rare earth material, ceria has wide applications in catalysis, electrochemistry, and optics due to its unique properties.^{1–9} For instance, CeO_2 can be used as a three-way catalyst (TWC) for exhaust gas treatment from automobiles because of its high oxygen storage capacity (OSC), associated with its rich oxygen vacancies and low redox potential between Ce^{3+} and Ce^{4+} .^{1–3} Ceria doped with other rare earth ions has high oxide ion conductivity at a comparable low temperature (about 600 °C) and thus has been applied in solid oxide fuel cells.^{4–7} CeO_2 also has strong absorption in the ultraviolet range and is hence used as ultraviolet (UV) blocking materials.^{8,9}

In recent years, the preparation and characterization of nanoparticulate oxide powders have attracted much attention for their considerably small sizes, high surface areas, and improved sintering properties in comparison with bulk materials. Some efforts have also been devoted to the synthesis of ultrafine CeO_2 powders by techniques such as thermal decomposition,¹⁰ flash combustion,¹¹ mechanochemical processing,¹² coprecipitation,^{6,13} homogeneous precipitation,^{14–17} electrochemical synthesis,¹⁸ and hydrothermal^{19–23} and solvothermal processes.^{24–26} More recently, Inoue et al. prepared a colloidal solution of 2 nm ceria particles by oxidation of cerium metal in 2-methoxyethanol under solvothermal condition.²⁷ Adachi

et al. obtained 2.6 and 4.1 nm ceria particles using reverse micelles.⁸ Gedanken et al. synthesized 3.3 nm CeO_2 ultrafine particles by sonochemical treatment.²⁸ Zhu et al. also fabricated 2.6 and 2.8 nm nanocrystalline ceria particles using sonochemical and microwave assisted heating methods.²⁹ So far, for the ceria nanoparticles, there were no general agreements on the grain size-dependent optical properties (UV absorption and band gap energy) due to the lack of a series of data collected for ceria nanoparticles with altered grain sizes in one research.^{8,27–29} Therefore, a deep understanding of the grain size-dependent optical properties of ceria is believed to have both academic and practical interests.

As a robust technique, solvothermal synthesis has extraordinary advantages of single step low-temperature synthesis, superior composition and morphological control, and powder reactivity over the other techniques in preparing lowly aggregated and highly crystallized nanomaterials. In addition, during the solvothermal treatment, the pressure in the autoclave can be readily adjusted to some extent by using various solvents, which have varying vapor pressure at a given temperature. For instance, at 100 °C, the pressures in the autoclave when water and ethanol are used as the solvents are about 1.0 and 2.5 atm, respectively, as the temperature is elevated to 180 °C, the corresponding pressures reach about 10 and 20 atm, respectively. Previously, some research was conducted to prepare oxide nanomaterials (CeO_2 , ZrO_2 , and TiO_2) by the alcohothermal

* Corresponding author. Fax: +86-10-6275-4179. E-mail: chyan@chem.pku.edu.cn.

method in pure ethanol, but the reaction mechanism (whether alcoholic or hydrolytic) still needs further clarification.^{26,30–32}

The motivations of this research are to exploit the alcohol-thermal method to prepare ceria nanocrystals with altered grain sizes through the addition of different bases, to understand the alcohol-thermal reaction mechanism, to reveal the correlation between the grain size and the band gap energies, and to examine the catalytic activity of the as-prepared ceria nanocrystals supported on γ -Al₂O₃ for CO conversion. The ceria samples were characterized by the techniques of powder X-ray diffraction (PXRD), X-ray photoelectron spectroscopy (XPS), transmission electron microscopy (TEM) and high-resolution TEM (HRTEM), nitrogen adsorption, thermogravimetry and differential thermal analysis (TG-DTA), Fourier transformation infrared spectroscopy (FT-IR), and ultraviolet and visible spectroscopy (UV–vis). In this paper, the facile alcohol-thermal synthesis, size-dependent UV absorption, and enhanced CO conversion activity of ceria nanocrystals are presented.

Experimental Section

1. Synthesis. Ce(NO₃)₃·6H₂O (A.R. grade, ≥99.0%) and (NH₄)₂Ce(NO₃)₆ (A.R. grade, ≥99.0%) were used as the sources of cerium, respectively. A given quantity (80 mL) of an ethanol solution of the cerium salt with a fixed concentration (0.05 mol L^{−1}) was poured into a Teflon bottle with an inner volume of 100 mL. KOH or NaOH powder in a given amount (0.008–0.32 mol) was slowly added into the above solution under stirring. After 20 min this Teflon bottle with the final concentration of base in the range 0.1–4 mol L^{−1} was then held in a stainless steel vessel and the vessel was sealed tightly. The alcohol-thermal treatment was performed at 180 °C for 24 h under autogenous pressure in an electric oven. As the autoclave cooled to room temperature, the precipitates were separated by centrifuging, washed with deionized water and ethanol, and then dried in a vacuum at 80 °C overnight. The products after drying were brown or yellow powders with high yields (77–93%). For convenience in discussion, the samples obtained from Ce(NO₃)₃·6H₂O with using KOH as the base were denoted as **K3** series and those obtained from (NH₄)₂Ce(NO₃)₆ as **K4** series.

For catalytic tests, some as-prepared ceria samples were loaded on γ -Al₂O₃ carrier with a surface area of 200 m² g^{−1} by the following steps: the as-synthesized CeO₂ powder after washing was directly mixed with γ -Al₂O₃ in the molar ratio 1/6 (CeO₂/ γ -Al₂O₃) in water. The above solution was stirred overnight; then the suspension was centrifuged and the catalyst powder was formed. The catalyst was washed successively with deionized water, dried, and preheated in air for 5 h before test.

2. Characterization Methods. The PXRD patterns were recorded on a Rigaku D/MAX-2000 diffractometer with a slit of 1/2° at a scanning rate of 4° min^{−1}, using Cu K α radiation (λ = 1.5406 Å). With the software “LAPOD” of least-squares refinement of cell dimensions from powder data by Cohen’s method,^{33,34} the lattice parameters were calculated. The average grain size D was estimated according to the Scherrer equation,³⁵

$$D = 0.90\lambda/\beta \cos \theta$$

where θ is the diffraction angle of the (111) peak and β is the full width at half-maximum (fwhm) of the (111) peak (in radians), which is calibrated from high-purity silicon. XPS measurements were carried out in an ion-pumped chamber (evacuated to 2×10^{-9} Torr) of an Escalad5 spectrometer, employing Mg K α radiation (BE = 1253.6 eV). The binding energy (BE) for the samples was calibrated by setting the measured BE of C1s to 284.6 eV. Particle sizes and morphol-

ogies were examined by transmission electron microscopy (TEM, 200CX, JEOL) operated at 160 kV. High-resolution TEM (HRTEM) characterization was performed with a Philips Tecnai F30 FEG-TEM operated at 300 kV. The BET specific surface area (S_{BET}) was measured by nitrogen adsorption at 78.3 K, using an ASAP 2010 analyzer (Micromeritics Co. Ltd.), and measurements were performed after outgassing the sample at 423 K for 4 h under vacuum, down to a residual pressure better than 10^{-3} Torr. The pore volume was calculated from the desorption branch of the isotherms, on the basis of the BJH method.³⁶ The combined TG-DTA runs were performed with a Universal V2.60 TA instrument at a heating rate of 5 °C min^{−1} from room temperature to 1000 °C, using α -Al₂O₃ as a reference. FT-IR spectra were obtained on a Nicolet Magna 750 FTIR spectrometer at a resolution of 4 cm^{−1} with a Nic-Plan IR microscope. Elemental analysis was carried out on an Elementar Vario EL system. The as-synthesized powder before drying was dispersed in ethanol at a concentration of around 10^{-3} mol L^{−1} and then sonicated at room temperature for 30 min, and a transparent colloidal solution was thus obtained. The UV–vis spectra of the above solutions were recorded on a HITACHI U-3010 spectrometer using a quartz cell (1 cm path length), and pure ethanol was used as a blank. The optical absorption coefficient α was calculated according to the following equation:

$$\alpha = (2.303 \times 10^3 A \rho)/lc$$

where A is the absorbance of a sample, ρ is the real density of CeO₂ (7.28 g cm^{−3}), l is the pathlength, and c is the concentration of the ceria suspensions.

The catalytic reactions for CO oxidation were carried out in a conventional fixed-bed quartz tube reactor (8.0 mm in outer diameter) between 423 and 673 K with feeding about 0.5 g of the catalyst. The inlet gas composition was 2% CO and 16% O₂ with He as balance, and the flow rate was kept at 25 mL min^{−1}. The catalytic products were analyzed by FT-IR spectrometer (Bruker Vector 22) for CO and gas chromatography (Beifen SQ-206) for O₂.

Results and Discussion

1. Characteristics of Ceria Nanocrystals. Figure 1 shows the PXRD patterns of the as-synthesized ceria powders. The broadening of the reflections in the diffractograms distinctly indicates the formation of nanocrystals. All the samples appeared in the same phase of pure fluorite cubic structure with lattice constants in the range 0.5402–0.5426 nm (JCPDS card no. 34-0394, a = 0.5411 nm, space group $Fm\bar{3}m$), no matter when they were derived from the Ce(III) or Ce(IV) source. The characteristics of the as-prepared ceria nanocrystals were summarized in Table 1.

With the concentration of KOH (C_{KOH}) increasing from 0.1 to 0.2 mol L^{−1}, the average grain size (D) of as-prepared ceria nanocrystals, calculated by the Sherrer formula, reduced from 5.0 to 2.6 nm. With C_{KOH} further raised to 4 mol L^{−1}, D of **K3** samples increased to 6.9 nm. When (NH₄)₂Ce(NO₃)₆ was used as the cerium source, the grain size dependence on the concentration of KOH for the **K4** series was observed to be similar to that for the **K3** series, except that the smallest D appeared at C_{KOH} = 0.5 mol L^{−1}. Wang et al. synthesized the CeO₂ nanocrystalline by the alcohol-thermal technique without addition of any bases, using Ce(NO₃)₃·6H₂O as the starting material, and the D value for the products remained 7 nm.²⁶ In the present work, D values of our ceria nanocrystals can be controlled between 2.6 and 6.9 nm via changing the amount of KOH.

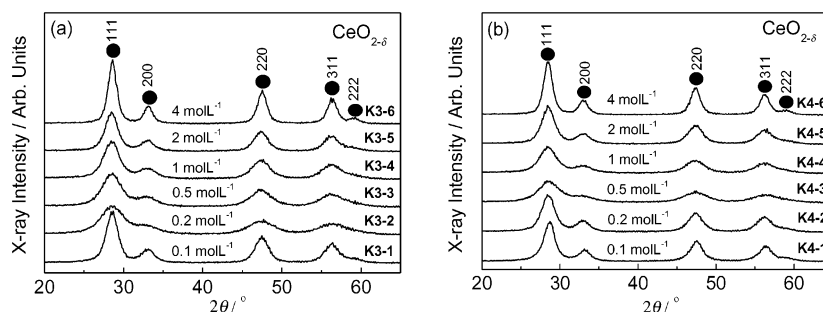


Figure 1. PXRD patterns of as-synthesized $\text{CeO}_{2-\delta}$ powders using (a) Ce(III) and (b) Ce(IV) salts as the starting materials under various KOH concentrations. Solid circles: peak of cubic CeO_2 .

TABLE 1: Color, Lattice Parameter (a), Average Grain Size (D), BET Specific Surface Area (S_{BET}), and Calculated Specific Surface Area (S_{cal}) of the K3 and K4 Series Samples Treated at Various KOH Concentrations (C_{KOH})

	K3-1	K3-2	K3-3	K3-4	K3-5	K3-6
$C_{\text{KOH}}/\text{mol L}^{-1}$	0.1	0.2	0.5	1	2	4
color	brown	brown	yellow	yellow	yellow	yellow
a/nm	0.5412(4)	0.5409(6)	0.5424(1)	0.5424(2)	0.5425(5)	0.5409(2)
D/nm	5.0	2.6	3.0	3.7	4.6	6.9
D^3/nm		10.3	8.1	7.7	6.9	8.5
D^3/D		4.0	2.7	2.1	1.5	1.2
$S_{\text{BET}}/\text{m}^2 \text{g}^{-1}$	140	175	197	184	154	128
$S_{\text{cal}}/\text{m}^2 \text{g}^{-1}$	165	317	275	223	179	115
$S_{\text{BET}}^a/\text{m}^2 \text{g}^{-1}$		54	34	100	137	107
$S_{\text{BET}}^a/S_{\text{BET}}$		0.31	0.17	0.54	0.89	0.84

	K4-1	K4-2	K4-3	K4-4	K4-5	K4-6
$C_{\text{KOH}}/\text{mol L}^{-1}$	0.1	0.2	0.5	1	2	4
color	brown	brown	brown	yellow	yellow	yellow
a/nm	0.5402(4)	0.5426(3)	0.5419(1)	0.5422(4)	0.5419(2)	0.5414(1)
D/nm	5.3	4.6	2.9	3.6	4.7	6.9
D^3/nm			9.1	6.4	7.0	8.3
D^3/D			2.7	2.1	1.5	1.2
$S_{\text{BET}}/\text{m}^2 \text{g}^{-1}$	108	103	238	226	178	136
$S_{\text{cal}}/\text{m}^2 \text{g}^{-1}$	155	179	284	229	175	119
$S_{\text{BET}}^a/\text{m}^2 \text{g}^{-1}$			69	160	147	126
$S_{\text{BET}}^a/S_{\text{BET}}$			0.29	0.71	0.83	0.93

^a Calcined at 500 °C for 2 h.

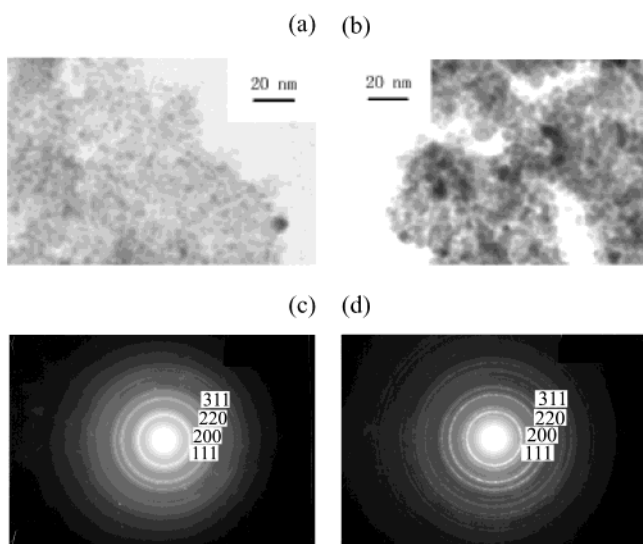


Figure 2. TEM micrographs of the ceria nanocrystals of (a) **K3-2** and (b) **K3-6**. SAED patterns of the ceria nanocrystals of (c) **K3-2** and (d) **K3-6**.

Figure 2 is the TEM micrographs and SAED patterns of **K3-2** and **K3-6**. It can be seen that the as-synthesized $\text{CeO}_{2-\delta}$ nanocrystals were both uniformly dispersed and weakly aggregated, and the average crystallite sizes of **K3-2** and **K3-6** were 2.5 and 6.5 nm, respectively, very consistent with their

XRD sizes (see Table 1). The SAED patterns of these two samples show that both consisted of cubic ceria nanocrystals, and **K3-6** (Figure 2d) showed better crystallinity than **K3-2** (Figure 2c). The HRTEM images of the above nanocrystals (Figure 3) reflect that adjacent nanocrystals of **K3-2** intruded on each other and the grain boundary was blurring to some degree. However, the grain boundary of **K3-6** was clear, indicating that it crystallized better and agglomerated less. From the HRTEM micrographs, the (111) facet with an interplanar spacing of about 0.32 nm can be identified for the as-prepared ceria nanocrystals.

As shown in Table 1, BET surface areas (S_{BET}) of **K3** and **K4** series samples can show the agglomerate interactions of the as-prepared ceria nanocrystals. When the amount of the base was raised, S_{BET} of either **K3** or **K4** series increased to a maximum value at $C_{\text{KOH}} = 0.2$ or 0.5 mol L^{-1} and then reduced to a minimum value at 4 mol L^{-1} , in opposition to the trend of grain sizes. The highest S_{BET} value of all the as-prepared ceria powders was $238 \text{ cm}^2 \text{g}^{-1}$ (**K4-3**), which exceeded that of the CeO_2 powders prepared by the hydrothermal method in the presence of urea ($80 \text{ m}^2 \text{g}^{-1}$),²³ the microemulsion method ($153\text{--}185 \text{ m}^2 \text{g}^{-1}$),⁸ and the sonochemical process ($227 \text{ m}^2 \text{g}^{-1}$).

29

We also calculated the theoretical specific surface area (S_{cal}) of these samples from D by the following formula: $S_{\text{cal}} = 6/(D\rho)$, where ρ is the theoretical density of CeO_2 (7.28 g cm^{-3}). From calculated results (see Table 1), it can be seen that the

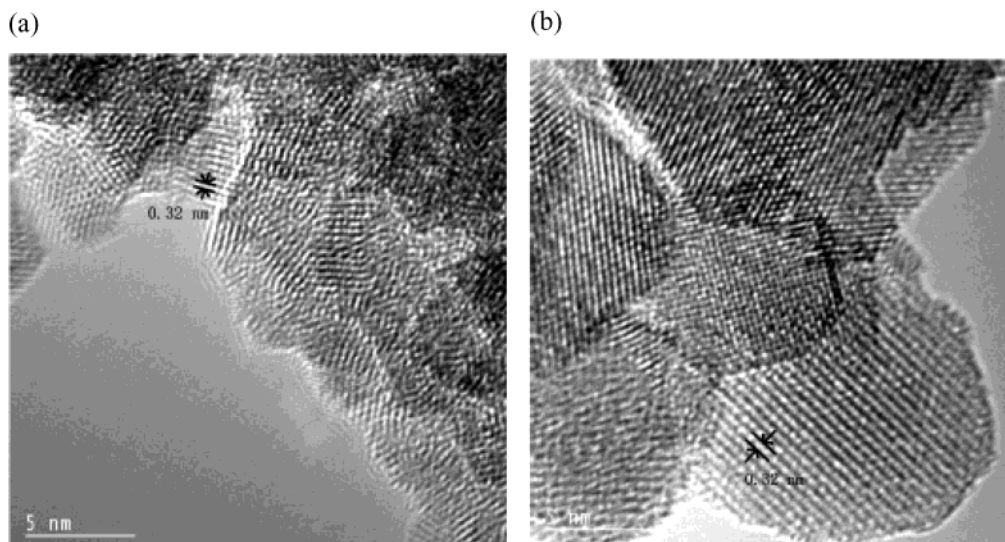


Figure 3. HRTEM images of the ceria nanocrystals of (a) **K3-2** and (b) **K3-6**.

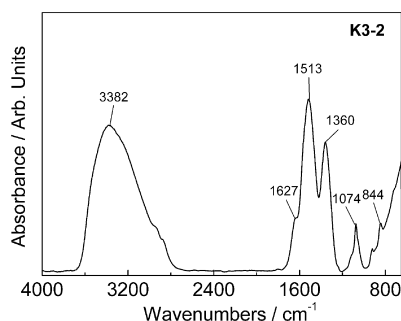


Figure 4. FT-IR spectrum of the sample **K3-2**.

values of S_{BET} and S_{cal} were basically consistent under the high base condition ($C_{\text{KOH}} = 1\text{--}4 \text{ mol L}^{-1}$) and showed a large deviation in low base samples ($C_{\text{KOH}} = 0.1\text{--}0.5 \text{ mol L}^{-1}$), especially for **K3-2**. This result could be explained by a higher degree of agglomeration favorable to the lower base powders. To verify this assumption, the samples with D varying from the minimum (**K3-2** or **K4-3**) to the maximum (**K3-6** or **K4-6**) were calcined at 500°C for 2 h in still air. Table 1 also shows D and S_{BET} of these powders after calcination. The average grain size of each sample increased after calcination, indicating that the nanocrystals coarsened and grew prominently upon calcination. However, the ratio of increase fell down (from 4.0 to 1.2 for **K3** series and from 3.1 to 1.2 for **K4** series) with the increasing amount of base, revealing that low base samples with calcination show a relatively high grain growth rate partially due to their relatively high degree of aggregations. The reduction of the ratio of S_{BET} before and after calcination decreased sharply when more KOH was added. The maximum S_{BET} value after calcination at 500°C was $160 \text{ m}^2 \text{ g}^{-1}$, higher than mesoporous ceria ($150 \text{ m}^2 \text{ g}^{-1}$)³⁷ and CeO_2 catalyst ($115 \text{ m}^2 \text{ g}^{-1}$),³⁸ which were calcined at 400°C .

Figure 4 is the typical FT-IR spectrum of **K3-2**. The broad band at 3382 cm^{-1} was due to O–H stretches of water associated with the powder. The bands at 1627 and 1513 cm^{-1} are ascribed to the bending mode of hydroxyl groups of adsorbed water and ethanol. The other three bands at 1360 , 1074 , and 844 cm^{-1} are attributed to the vibrations associated with uncoordinated NO_3^- ions. By elemental analysis, the contents of the impurity elements including N, C, and H in this sample were determined as 0.35, 1.21, and 1.25 wt %, respectively, indicating the presence of a trace amount of adsorbed NO_3^-

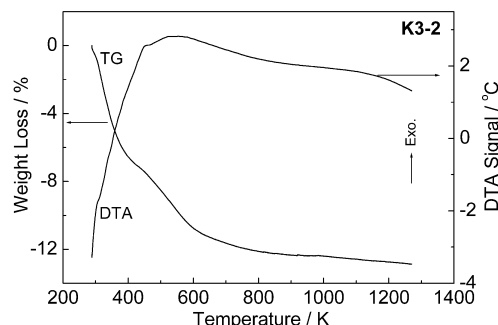


Figure 5. Combined TG-DTA run of the sample **K3-2**.

and ethanol plus some absorbed water in the as-synthesized **K3-2** product. Due to the high degree of interagglomeration of nanocrystals via hydrogen bonding and van der Waals force, low base samples absorbed more solvents and impurities than high base ones. With increasing C_{KOH} from 0.2 to 4 mol L^{-1} , the impurities could be reduced to a certain degree. For the sample **K3-6**, N, C, and H contents were decreased to 0.29, 0.80, and 0.63 wt %, respectively. The reduced impurities for high base samples were also confirmed by TG-DTA analysis (typically see Figure 5). Both **K3-2** and **K3-6** lose the absorbed species step by step from room temperature to about 600°C , but the total loss of weight was 12.4% for **K3-2** and 4.9% for **K3-6**. No exothermic peak associated with amorphous to cubic transition ($250\text{--}280^\circ\text{C}$)³⁹ existed below 1000°C in each sample, revealing that the as-prepared ceria nanocrystals were highly crystallized after alcoholthermal treatment at 180°C .

2. XPS Analysis. Figure 6 typically depicts the XPS spectra of the as-synthesized ceria nanocrystals. Peaks of Ce3d, O1s, C1s and Ce4d can be identified for **K3-2** and **K4-3** from Figure 6a. The peak at 284.6 eV was attributed to ethanol and/or CO_2 adsorbed on the surfaces of the as-obtained ceria nanocrystals. No peaks ascribable to K2p and N1s are observed, indicating that the KNO_3 impurity was in trace amount.

From Figure 6b, we can find that six Ce3d binding energy (BE) peaks for **K3** and **K4** series samples were consistent with the previous report of Ce^{4+} ,⁴⁰ indicating the main valence of cerium in these samples was +4, regardless of the valences of the starting cerium salts. Therefore, the molecular formula of as-prepared ceria nanocrystals should be expressed as $\text{CeO}_{2-\delta}$, where δ represents the number of oxygen vacancies. Strikingly,

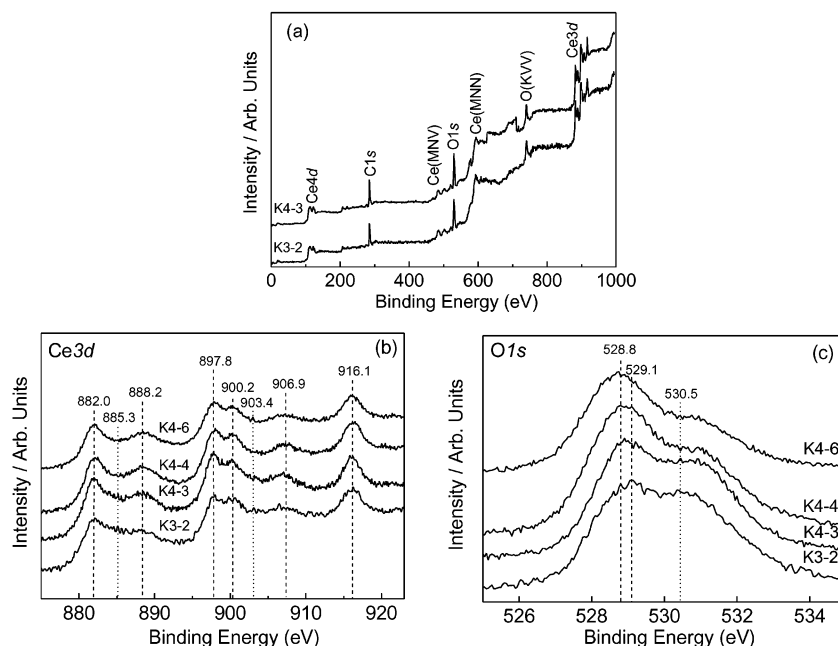
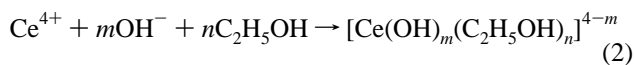
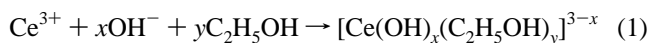


Figure 6. XPS patterns of ceria samples: (a) survey spectra; (b) Ce3d; (c) O1s.

the spectrum of **K3-2** appears more intense in the BE of 885.3 and 903.4 eV (characteristic peaks of Ce_2O_3), compared to **K4** series samples, revealing **K3-2** contained more Ce^{3+} . For the **K4** series samples, no apparent increase of Ce^{3+} content was observed when the grain size was reduced from 6.9 nm for **K4-6** to 2.9 nm for **K4-3** (see Figure 6b).

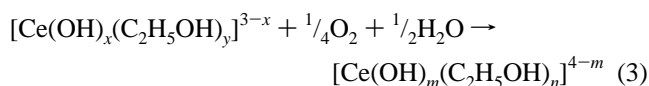
From Figure 6c, it is noted that the O1s spectra of the four samples consist of two BE peaks: one at 530.5 eV, originated from absorbed oxygen, and another standing at a lower BE, attributable to lattice oxygen. The BE increase of O1s in **K3-2** (529.1 eV), compared to **K4** series samples (528.8 eV), also indicates its greater Ce^{3+} component.

3. Alcoholthermal Mechanism. Prior to alcoholthermal treatment, when base (KOH) was added to the mother liquors, both **K3** and **K4** series solutions were turbid with the formation of colloidal precipitates. The color of the precipitates for the **K4** series was yellow, whereas that for the **K3** series was first light brown, then dark brown, and finally light yellow. In analogy with hydrolysis of the cerium ion in water,²¹ the above colloidal precipitates were thought to be polymers of cerium hydroxide coordinated with ethanol through the following reactions:

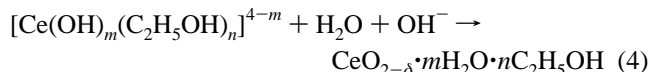


($x + y$ and $m + n$ equal to the coordination number of cerium ion).

Meanwhile, the mixture of Ce^{3+} salt with base under room temperature contained a step of $\text{Ce}^{3+}/\text{Ce}^{4+}$ transfer, which was preferred in high base solution.²¹ Thus, the main valence of cerium in **K3** solution before alcoholthermal treatment was +4, based on the color change of the reaction solution. The $\text{Ce}^{3+}/\text{Ce}^{4+}$ transfer process can be expressed by the following equation:



In addition, a part of the hydroxides may be transferred to hydrated and alcoholized $\text{CeO}_{2-\delta}$ by the following equation:³⁹



On the basis of the TEM coupled with SAED analysis typically shown in Figure 1S, we see that the colloidal precipitates of **K3** series were crystallized to some extent, whereas those of the **K4** series were mainly amorphous. To attain full crystallization via a dissolution and recrystallization mechanism, water was required in the above reactions. However, water was scarce in the starting solutions. It is about 0.43 or 0.13 mol L^{-1} H_2O in the **K3** or **K4** series solutions, respectively, if considering 0.3% H_2O in ethanol (A.R. grade) and six crystal waters in $\text{Ce}(\text{NO}_3)_3 \cdot 6\text{H}_2\text{O}$.

When the above colloidal precipitates were subjected to alcoholthermal treatment, reaction 4 can be accelerated due to the supply of extra H_2O through the reaction between ethanol and base under alcoholthermal conditions at 180 °C:



To estimate the effects of the addition of KOH on the crystallization mechanism of ceria nanocrystals during the alcoholthermal treatment, 0.05 mol L^{-1} $\text{Ce}(\text{NO}_3)_3 \cdot 6\text{H}_2\text{O}$ and 0.2 mol L^{-1} KOH were mixed in 80 mL of ethanol under stirring. The precipitate was separated, washed, dried, and then heat-treated at 300 °C in air for 1 h to remove water completely. This powder was alcoholthermally treated at 180 °C for 24 h in pure ethanol or an ethanol solution of 4 mol L^{-1} KOH, respectively. The PXRD results of the above samples are shown in Figure 7. It can be seen that three main diffracted peaks of cubic ceria appeared in pattern a, indicating the colloidal precipitate in room temperature was partly crystallized, as also confirmed by SAED analysis previously (Figure 1S). The average grain size of powder c (first heat-treated at 300 °C for 1 h and then alcoholthermally treated in the absence of KOH) was about 4.6 nm, the same as powder b (heat-treated at 300 °C for 1 h), whereas D of powder d rose to 9.1 nm (first heat-

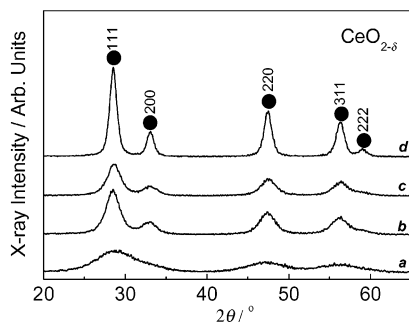
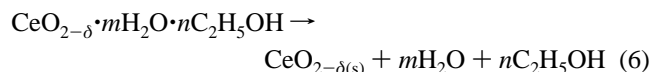


Figure 7. PXRD patterns of the as-prepared $\text{CeO}_{2-\delta}$ powders: (a) colloidal precipitate produced from 0.05 mol L^{-1} $\text{Ce}(\text{NO}_3)_3$ in 0.2 mol L^{-1} KOH ethanol solution before alcohothermal treatment; (b) product after heat treatment of (a) at 300°C for 1 h; (c) product after alcohothermal treatment of (b) in pure ethanol solution at 180°C for 24 h; (d) product after alcohothermal treatment of (b) powder in 4 mol L^{-1} KOH ethanol solution at 180°C for 24 h.

treated at 300°C for 1 h and then alcohothermally treated in the presence of 4 mol L^{-1} KOH). Therefore, with the addition of KOH, more water was produced and the basicity was enhanced under alcohothermal conditions, which in turn made the $\text{CeO}_{2-\delta}$ nanocrystals grow larger and crystallize better via the hydrolytic mechanism.

The important effects of KOH can be further understood from Figure 1 and Table 1. When $C_{\text{KOH}} \geq 1 \text{ mol L}^{-1}$, the as-synthesized $\text{CeO}_{2-\delta}$ nanocrystals were better crystallized (Figure 1a) and D was larger (Table 1) than that for the low base samples ($C_{\text{KOH}} \leq 1 \text{ mol L}^{-1}$). It is concluded that the size of $\text{CeO}_{2-\delta}$ nanocrystals can be controlled in the range 2.6–6.9 nm by adding different amounts of KOH in the present work.

Through the hydrolytic mechanism in alcohothermal treatment, $\text{CeO}_{2-\delta}$ nanocrystals can obtain full crystallization according to the following reaction:



Apparently, reaction 6 is the subsequence of (4). Totally, the less water produced in the reaction solution, the more species absorbed onto cerium ion to inhibit the growth of $\text{CeO}_{2-\delta}$ nanocrystals, which can also be inferred from the altered degree of agglomeration for the low base and high base samples on the basis of the results of HRTEM (Figure 3), nitrogen adsorption (Table 1), and TG measurements (Figure 5).

From Table 1, we can also see that the D minimum of $\text{CeO}_{2-\delta}$ powder emerged when $C_{\text{KOH}} = 0.2 \text{ mol L}^{-1}$ (**K3** series) or 0.5 mol L^{-1} (**K4** series), not at the C_{KOH} minimum (0.1 mol L^{-1}). It can be explained by the combined actions of two roles played by KOH. One role is producing hydroxide ion to form cerium hydroxide, and another is offering extra water to form hydrated $\text{CeO}_{2-\delta}$ through reaction 5. With the increase of C_{KOH} , more hydroxide was created (eq 1) and more water was required to obtain $\text{CeO}_{2-\delta}$ nanocrystals according to reaction 4. For example, with $\text{Ce}(\text{III})$ nitrate as the starting material, when $C_{\text{KOH}} \leq 0.2 \text{ mol L}^{-1}$, KOH only acted as the former role (namely producing OH^-) and the amount of H_2O in solution was rather low and was nearly kept as a constant (0.43 mol L^{-1}). When $C_{\text{KOH}} < 0.2 \text{ mol L}^{-1}$, the amount of KOH was insufficient to precipitate the cerium ions completely. Upon alcohothermal treatment, some of the unprecipitated cerium ions will be forced to hydrolyze, and thus a weak acidic environment will be generated. When $C_{\text{KOH}} = 0.2 \text{ mol L}^{-1}$, the amount of KOH can fairly precipitate the cerium ions completely, and a neutral

pH will be reached. Possibly due to a decrease in the nucleation in the acidic solution, ^{23}D at $C_{\text{KOH}} = 0.1 \text{ mol L}^{-1}$ was larger than that at $C_{\text{KOH}} = 0.2 \text{ mol L}^{-1}$ (see Table 1). When $C_{\text{KOH}} \geq 0.2 \text{ mol L}^{-1}$, the amount of hydroxide ions was enough to precipitate all the cerium ions due to the saturation of coordination. When C_{KOH} was further raised, more extra water was created and the basicity was gradually enhanced; in this case, the grain growth was accelerated via the dissolution and precipitation mechanism and the $\text{CeO}_{2-\delta}$ nanocrystals gained better crystallization. Consequently, the minimum average grain size of $\text{CeO}_{2-\delta}$ powder emerged at $C_{\text{KOH}} = 0.2 \text{ mol L}^{-1}$. Similar results were also obtained when $\text{Ce}(\text{IV})$ was used as starting material or NaOH was used as the source of base (see Tables 1 and 1S).

From Table 1S, we also see that the variety of base played a crucial role in the formation of ceria nanocrystals upon alcohothermal treatment. If KOH was replaced by NaOH (a relatively weak base in ethanol), the grain size of $\text{CeO}_{2-\delta}$ nanocrystals became larger, especially for high base samples (See Table 1S). It can be deduced that stronger base in the reaction solution led to the accelerated nucleation and the reduction of grain size upon alcohothermal aging. Thus, using different starting bases can also control the size of $\text{CeO}_{2-\delta}$ particles during the alcohothermal reaction employed.

Experimentally, we also observed that an uncomfortable smell escaped from the Teflon bottles and the color of the reaction solution was brown in low base samples after alcohothermal treatment. This may result from the oxidation of ethanol by Ce^{4+} under alcohothermal conditions, but further investigation is required.

4. Size-Dependent UV Absorption Spectra and Band Gap Energies. To reveal the correlation between the band gap energies and the grain sizes for the as-prepared ceria nanocrystals, their UV spectra were measured in ethanol suspensions (Figure 2S). Figure 8a shows the typical absorption spectra of **K3-2** ($D = 2.6 \text{ nm}$) and **K4-3** ($D = 2.9 \text{ nm}$). The spectra distinctly exhibited a strong absorption band at the UV region due to the charge-transfer transitions from $\text{O}2p$ to $\text{Ce}4f$ and block damage by UV radiation. However, no absorption was detected above 500 nm in wavelength.

The plots of $(\alpha h\nu)^2$ vs photon energy of **K3-2** and **K4-3** are shown in Figure 8b, where α is the absorption coefficient and $h\nu$ is photon energy. For direct transitions, α near the absorption edge can be expressed in the following equation⁴¹

$$\alpha \propto (h\nu - E_d)^{1/2}/h\nu$$

where E_d is the band gap energy for direct transitions. The intersection of the extrapolated linear portions gives the direct band gap energy (E_d) and the value was 3.43 eV for **K3-2** and 3.33 eV for **K4-3**. These values are consistent with ceria nanoparticles synthesized by micromulsion method (3.44 eV for 2.6 nm and 3.38 eV for 4.1 nm).⁸

For indirect interband transitions, α near the absorption edge follows the equation⁴¹ given by

$$\alpha \propto (h\nu + E_p - E_i)^2 / (e^{h\nu/kT} - 1) + (h\nu - E_p - E_i)^2 e^{h\nu/kT} / (e^{h\nu/kT} - 1)$$

where E_i is the band gap energy for indirect transitions and E_p is the phonon energy, k is Boltzmann constant, and T is the absolute temperature. The plots of $\alpha^{1/2}$ vs photon energy for the above two samples are shown in Figure 8c, and the intersection of the extrapolated linear portions gives the indirect

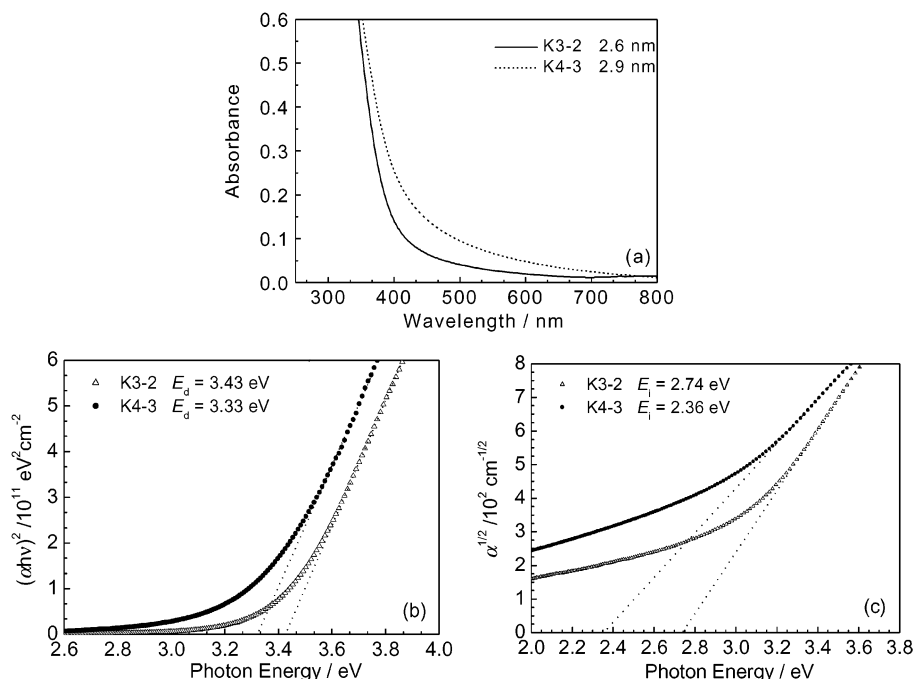


Figure 8. (a) UV-vis spectra of as-prepared $\text{CeO}_{2-\delta}$ nanocrystals of **K3-2** and **K4-3** dispersed in ethanol. (b) Plots of $(\alpha h\nu)^2$ vs photon energy for **K3-2** and **K4-3**. (c) Plots of $\alpha^{1/2}$ vs photon energy for **K3-2** and **K4-3**.

TABLE 2: Average Grain Size, Direct Band Gap Energy (E_d), and Indirect Band Gap Energy (E_i) of the K3 and K4 Series Samples Treated at Various KOH Concentrations

	K3-2	K3-3	K3-4	K3-5	K3-6
D/nm	2.6	3.0	3.7	4.6	6.9
E_d/eV	3.42(1) ^a	3.43(2)	3.44(1)	3.42(1)	3.38(1)
E_i/eV	2.73(1)	2.76(2)	2.74(2)	2.70(2)	2.56(4)

	K4-3	K4-4	K4-5	K4-6
D/nm	2.9	3.6	4.7	6.9
E_d/eV	3.30(2)	3.32(3)	3.33(2)	3.28(1)
E_i/eV	2.34(1)	2.48(8)	2.49(3)	2.31(3)

^a Number in bracket is the standard error.

band gap energy (E_i). The E_i value was 2.74 eV for **K3-2** and 2.36 eV for **K4-3**. These values also basically agree with those for ceria nanoparticles synthesized by the micromulsion method (2.87 eV for 2.6 nm and 2.73 eV for 4.1 nm).⁸ All the direct or indirect band gap energies determined for our $\text{CeO}_{2-\delta}$ nanocrystals with different D are given in Table 2, which are a bit smaller than those determined for oriented polycrystalline ceria ($E_d = 3.6 \text{ eV}$ and $E_i = 3.2 \text{ eV}$) by spectroscopic ellipsometry measurement.⁴²

Because our ceria nanocrystals are nontextured, compared to nonoriented polycrystalline CeO_2 ($E_d = 3.19 \text{ eV}$ determined by UV-vis spectroscopy),⁴³ **K3** and **K4** series nanocrystals showed an increased E_d by a value exceeding 0.19 and 0.08 eV, respectively, due to the quantum size effect. The blue-shifting in the UV absorption spectra of CeO_2 nanocrystals has attracted much interest of many researchers in recent years.^{8,27-29} Generally, the absorption of ceria in the UV region originated from charge-transfer transition between O2p and Ce4f bonds, which overruns the well-known f to f spin-orbit splitting of the Ce4f state.^{44,45} It was theoretically deduced that the value of blue-shifting resulting from the reduction of particle size is inverse proportional to the square of the size due to quantum confinement effect. Some previous work reported the quantum size effect in the ceria system, but too few grain size data points have made the observations of this effect for ceria nanocrystals still in arguments.^{8,27-29} Figure 9 is the plot of energy band

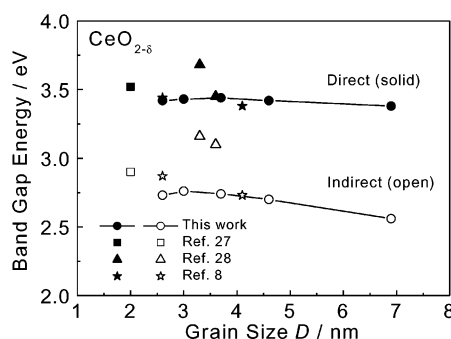


Figure 9. Plots of band gap energy vs average grain size for the as-prepared $\text{CeO}_{2-\delta}$ nanocrystals with using Ce(III) salt as the starting material.

gap vs average grain size for the as-prepared $\text{CeO}_{2-\delta}$ nanocrystals with Ce(III) salt as the starting material, wherein some data points taken from the literature were also included. In our work, the direct band gap energy (E_d) was increased by a value of about 0.05 eV when the grain size was reduced from 6.9 to 4.6 nm for the **K3** series and from 6.9 to 4.7 nm for the **K4** series, indicating the existence of quantum confinement effect for our ceria nanocrystals. For ensuring the reliability of our experiment data, each band gap energy value was determined by two independent measurements with the samples prepared in different Teflon bottles. The standard deviation of the band gap energy is quite small, not exceeding 0.02 eV, indicating the good repetition of the UV absorption measurements and the reliability of the band gap energies determined. To test the stability of the colloidal solution measured, the solution stood for at least 1 day. Strikingly, no precipitation took place, and the determined value of E_d or E_i remained unchanged. Therefore, the blue-shifting appearing in the UV spectra in our $\text{CeO}_{2-\delta}$ nanocrystals indeed was due to the quantum size effect.

However, the band gap energies remained nearly unchanged when the grain size was smaller than 4.0 nm, possibly due to both the quantum confinement and dielectric confinement effects. In the present case, the smaller the grain size of the ceria nanocrystals, the higher the degree of agglomeration and

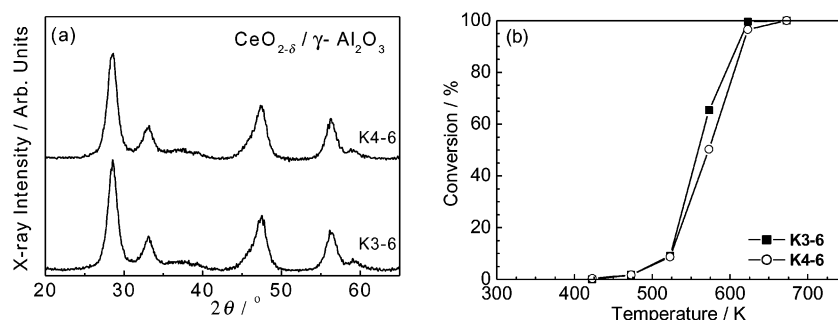


Figure 10. Characteristics of the as-synthesized CeO_{2-δ}/γ-Al₂O₃ catalysts: (a) PXRD patterns of the catalysts; (b) catalytic activities for CO oxidation.

the more hydroxyl groups adsorbed onto the surfaces of the nanocrystals, which was verified by the former combined results of TEM, FT-IR, and TG-DTA analysis. The modified surfaces of the as-prepared ceria nanocrystals might lead to the formation of a surface state energy band, which caused the adsorption at longer wavelengths. Under this condition, blue-shifting in the UV absorption caused by the quantum confinement effect may be counteracted by the red-shifting due to the dielectric confinement effect, which is inversely proportional to grain size. As a result, the band gap energies of our ceria nanocrystals remained nearly unchanged when the grain size was less than 4.0 nm.

To verify the existence of the dielectric confinement effect in the present experiments, we measured the UV-vis spectra of the **K4-4** sample ($D = 3.6$ nm) dispersed in pure ethanol and in 0.001 mol L⁻¹ KOH/ethanol solutions (Figure 3S) after stirring for more than 8 h. It is found that the **K4-4** sample showed a considerable red-shifting in the UV range when suspended in 0.001 mol L⁻¹ KOH/ethanol solution, and E_d and E_i displayed remarkable reduction down to 3.16 and 1.96 eV, respectively. This result indicated that the adsorption of trace KOH indeed could modify the surface state of the as-prepared nanocrystals and caused the red-shifting due to dielectric confinement effect. A similar phenomenon was ever observed for TiO₂ ultrafine particles.⁴⁶

Furthermore, it can be seen that the mean direct band gap energy of **K3** series (3.42 eV) was 0.11 eV larger than the **K4** series (3.31 eV). This difference may be attributed to the distinct valence conditions of different samples. **K3** series contained more Ce³⁺ than **K4** series observed from XPS spectra. The change from Ce⁴⁺ to Ce³⁺ was confirmed to increase the charge-transfer gap between O2p and Ce4f bonds.⁴⁴ Therefore, E_d of CeO_{2-δ} nanocrystals increased when more Ce³⁺ component was included.

From Table 2, we can see that both the direct and indirect band gap energy showed the same dependence on the grain size of as-prepared CeO_{2-δ} nanocrystals, indicating the charge-transfer transition in CeO_{2-δ} is not only direct but also indirect, which disagrees with a previous report.⁴⁴

5. CO Conversion Activity of Ceria Nanocrystals Supported on γ-Al₂O₃. To observe the catalytic activities of our CeO_{2-δ} nanocrystals for CO oxidation, the samples of **K3-6** and **K4-6** showing good crystallinity and the least reduction of surface area before and after calcination at 500 °C (see Figure 1 and Table 1) were selected as the sources of catalysts supported on γ-Al₂O₃. PXRD patterns of the **K3-6** and **K4-6** CeO_{2-δ}/γ-Al₂O₃ catalysts (Figure 10a) showed diffraction peaks assigned to CeO₂ (cubic) and γ-Al₂O₃, and there were no clear differences in the phase compositions between the two catalysts.

During the catalytic activity tests, CO₂ was the only product for both catalysts. In this research, the activities of CeO_{2-δ}/γ-

TABLE 3: BET Specific Surface Area, BJH Pore Volume, and Activity Data for the Selected Catalysts

sample	preheat temp/K	BET surf area/m ² g ⁻¹	BJH pore vol/cm ³ g ⁻¹	T_{con}^a /K
CeO _{2-δ} /Al ₂ O ₃ (K3-6)	423	196	0.45	559
CeO _{2-δ} /Al ₂ O ₃ (K4-6)	423	195	0.43	572

^a Temperature for 50% conversion of CO to CO₂.

Al₂O₃ catalysts were compared by the temperature at where 50% CO was converted to CO₂ (T_{con}). The activity results are shown in Table 3 and Figure 10b. The 50% conversion temperature of catalyst obtained from **K3-6** was 559 K, which was very close to that reported for the ceria nanocrystals prepared by the reverse micelles method (543 K).⁸ And the 50% conversion temperature of the catalyst from **K4-6** (572 K) was somewhat higher than that of **K3-6**, indicating its relatively low catalytic activity. Although their surface areas were almost the same, the catalyst from **K3-6** contained more oxygen vacancies than **K4-6**, which could be deduced from the previous characteristic results, and thus showed higher activity for CO oxidation.

It is well-known that ceria shows high oxidation ability due to its high oxygen vacancies and a low redox potential between Ce³⁺ and Ce⁴⁺. Possibly due to that, surface areas and the concentration of the defects (such as oxygen vacancies) were remarkably increased when the particle size was decreased to nanometer scale, the 50% conversion temperature of the as-prepared CeO_{2-δ}/Al₂O₃ catalysts was pronouncedly reduced compared to that of the bulk catalysts prepared by the coprecipitation route (593 K),⁸ indicating that our ceria nanocrystals possessed high catalytic activity for CO conversion.

Conclusion

Uniform CeO_{2-δ} nanocrystals with controllable sizes between 2.6 and 6.9 nm were prepared by the alcoholthermal method with the addition of base (KOH or NaOH), using Ce(III) or Ce(IV) salt as a starting material. The alcoholthermal method employed exhibited a hydrolytic mechanism. During the synthesis process, the starting base reacted with the solvent molecule (ethanol) to create extra water, which played an important role in the crystallization of CeO_{2-δ} nanocrystals via dissolution and recrystallization. CeO_{2-δ} nanocrystals were highly crystallized and well dispersed for high base samples yet conglomerated to some degree for low base samples, which can be seen from TEM and HRTEM micrographs, BET specific surface areas, and TG-DTA results. The CeO_{2-δ} nanocrystals had higher BET specific surface areas without calcination (238 m² g⁻¹) and with calcination (160 m² g⁻¹) than the previous reports. XPS spectra showed more Ce(III) for the samples prepared from Ce(NO₃)₃·6H₂O than for those from (NH₄)₂Ce(NO₃)₆. The blue-shifting in the UV absorption spectra was observed for the CeO_{2-δ}

nanocrystals for both direct and indirect band gap energies in the range of 4–7 nm due to quantum size effect. The band gap energies were almost unchanged for our ceria nanocrystals with sizes less than 4 nm probably because the blue-shifting due to the quantum size effect was counteracted by the red-shifting due to the dielectric confinement effect. Catalytic activity tests showed that the 50% conversion temperature of CO oxidation was down to 559 K for the $\text{CeO}_{2-\delta}/\gamma\text{-Al}_2\text{O}_3$ catalyst, lower than the conventional catalysts (593 K), possibly on account of the increased surface areas and rich oxygen vacancies (namely high OSC) of the $\text{CeO}_{2-\delta}$ nanocrystals.

Acknowledgment. We gratefully acknowledge the financial aid from NSFC (Nos. 20171003, 20221101, and 20023005), MOST of China (G19980613), Founder Foundation of PKU. We also appreciate Prof. Qin-Lin Guo and Prof. Kan Xie (Institute of Physics, CAS) for their great help with XPS measurements.

Supporting Information Available: Comparison of the average grain size and BET surface area of the samples obtained from different bases (KOH or NaOH) (Table 1S), TEM micrographs and SAED patterns of the colloidal ceria precipitates before alcoholothermal treatment (Figure 1S), scale-enlarged domain (320–460 nm) in the UV–vis spectra of different $\text{CeO}_{2-\delta}$ particles dispersed in ethanol (Figure 2S), and UV–vis spectra and band gap energy determination of as-prepared $\text{CeO}_{2-\delta}$ nanocrystals of **K4–4** dispersed in pure ethanol and 0.001 mol L^{-1} KOH/ethanol solution are available free of charge via the Internet at <http://pubs.acs.org>.

References and Notes

- (1) Powell, B. R.; Bloink, R. L.; Erckel, C. C. *J. Am. Ceram. Soc.* **1988**, *71*, 104.
- (2) Rao, G. R.; Fornasiero, P.; Di Monte, R.; Kaspar, J.; Vlaic, G.; Alducci, G. B.; Meriani, S.; Gubitosa, G.; Cremona, A.; Graziani, M. *J. Catal.* **1996**, *162*, 1.
- (3) Fornasiero, P.; Balducci, G.; Di Monte, R.; Kaspar, J.; Sergio, V.; Gubitosa, G.; Ferrero, A.; Graziani, M. *J. Catal.* **1996**, *164*, 173.
- (4) Kudo, T.; Obayashi, H. *J. Electrochem. Soc.* **1975**, *122*, 42.
- (5) Kudo, T.; Obayashi, H. *J. Electrochem. Soc.* **1976**, *123*, 415.
- (6) Yahiro, H.; Baba, Y.; Eguchi, K.; Arai, H. *J. Electrochem. Soc.* **1988**, *135*, 2077.
- (7) Herle, V.; Horita, T.; Kawata, T.; Sakai, N.; Yokokawa, H.; Dokiya, M. *J. Am. Ceram. Soc.* **1997**, *80*, 933.
- (8) Masui, T.; Fujiwara, K.; Machida, K.-I.; Adachi, G.-Y. *Chem. Mater.* **1997**, *9*, 2197.
- (9) Li, R. X.; Yabe, S.; Yamashita, M.; Momose, S.; Yoshida, S.; Yin, S.; Sato, T. *Solid State Ionics* **2002**, *151*, 235.
- (10) Janos, P.; Petrak, M. *J. Mater. Sci.* **1991**, *26*, 4062.
- (11) Sekar, M. M. A.; Manoharan, S. S.; Patil, K. C. *J. Mater. Sci. Lett.* **1990**, *9*, 1205.
- (12) Tsuzuki, T.; McCormick, P. G. *J. Am. Ceram. Soc.* **2001**, *84*, 1453.
- (13) Kirk, T. J.; Winnick, J. *J. Electrochem. Soc.* **1993**, *140*, 3494.
- (14) Matijevic, E.; Hsu, W. P. *J. Colloid Interface Sci.* **1987**, *118*, 506.
- (15) Aiken, B.; Hsu, W. P.; Matijevic, E. *J. Am. Ceram. Soc.* **1988**, *71*, 845.
- (16) Chen, P. L.; Chen, I.-W. *J. Am. Ceram. Soc.* **1993**, *76*, 1577.
- (17) Chu, X.; Chung, W.; Schmidt, L. D. *J. Am. Ceram. Soc.* **1993**, *76*, 2115.
- (18) Zhou, Y.; Philips, R. J.; Switzer, J. A. *J. Am. Ceram. Soc.* **1995**, *78*, 981.
- (19) Tani, E.; Yoshimura, M.; Somya, S. *J. Mater. Sci. Lett.* **1982**, *1*, 461.
- (20) Zhou, Y. C.; Rahaman, M. N. *J. Mater. Res.* **1993**, *8*, 1680.
- (21) Hirano, M.; Kato, E. *J. Am. Ceram. Soc.* **1996**, *79*, 777.
- (22) Hirano, M.; Kato, E. *J. Mater. Sci. Lett.* **1996**, *8*, 1249.
- (23) Hirano, M.; Kato, E. *J. Am. Ceram. Soc.* **1999**, *82*, 786.
- (24) Verdon, E.; Devalette, M.; Damazeau, G. *Mater. Lett.* **1995**, *25*, 127.
- (25) Wang, C. Y.; Zhang, W. Y.; Qian, Y. T. *Mater. Sci. Eng., B* **2002**, *94*, 170.
- (26) Wang, C. Y.; Qian, Y. T.; Xie, Y.; Wang, C. S.; Yang, L. G.; Zhao, W. *Mater. Sci. Eng., B* **1996**, *39*, 160.
- (27) Inoue, M.; Kimura, M.; Inui, T. *Chem. Commun.* **1999**, 957.
- (28) Yin, L. X.; Wang, Y. Q.; Pang, G. S.; Kolytyn, Y.; Gedanken, A. *J. Colloid Interface Sci.* **2002**, *246*, 78.
- (29) Wang, H.; Zhu, J. J.; Zhu, J. M.; Liao, X. H.; Xu, S.; Ding, T.; Chen, H. Y. *Phys. Chem. Chem. Phys.* **2002**, *4*, 3794.
- (30) Zhang, Y. W.; Xu, G.; Yan, Z. G.; Yang, Y.; Liao, C. S.; Yan, C. H. *J. Mater. Chem.* **2002**, *12*, 970.
- (31) Zhao, J. P.; Fan, W. H.; Wu, D.; Sun, Y. H. *J. Mater. Res.* **2000**, *15*, 402.
- (32) Wang, C.; Deng, Z. X.; Zhang, G. H.; Fan, S. S.; Li, Y. D. *Powder Technol.* **2002**, *125*, 39.
- (33) Langford, J. I. *J. Appl. Crystallogr.* **1971**, *4*, 259.
- (34) Langford, J. I. *J. Appl. Crystallogr.* **1973**, *6*, 190.
- (35) Guinier, A. *Theorie et Technique de la Radiocristallographie*, 3rd ed.; Dunod: Paris, 1964; p 482.
- (36) Barrett, E. P.; Joyner, L. G.; Halenda, P. H. *J. Am. Chem. Soc.* **1951**, *73*, 373.
- (37) Lundberg, M.; Skarman, B.; Cesar, F.; Wallenberg, L. R. *Micropr. Mesopor. Mater.* **2002**, *54*, 97.
- (38) Perrichon, V.; Laachir, A.; Abouarnadasse, S.; Touret, O.; Blanchard, G. *Appl. Catal., A* **1995**, *129*, 69.
- (39) Djuricic, B.; Pickering, S. J. *Eur. Ceram. Soc.* **1999**, *19*, 1925.
- (40) Paparazzo, E.; Ingo, G. M.; Zaccchetti, N. *J. Vac. Sci. Technol., A* **1991**, *9*, 1416.
- (41) Van Leeuwen, R. A.; Huang, C.-J.; Kammler, D. R.; Switzer, J. A. *J. Phys. Chem. B* **1995**, *99*, 15247.
- (42) Guo, S.; Arwin, H.; Jacobsen, S. N.; Järendahl, K.; Helmersson, U. *J. Appl. Phys.* **1995**, *77*, 5396.
- (43) Orel, Z. C.; Orel, B. *Phys. Status Solidi B* **1994**, *186*, K33.
- (44) Tsunekawa, S.; Fukuda, T. *J. Appl. Phys.* **1999**, *87*, 1318.
- (45) Tsunekawa, S.; Sahara, R.; Kawazoe, Y.; Kasuya, A. *Mater. Trans., JIM* **2000**, *41*, 1104.
- (46) Zhu, Y. C.; Ding, C. X. *J. Solid State Chem.* **1998**, *139*, 124.